International Forum on Aeroelasticity and Structural Dynamics
IFASD 2026
17-21 June 2026, Goettingen, Germany

ACTUATOR-FRIENDLY FLUTTER CONTROL DESIGN USING ROBUST CONTROL AND BLENDING OF INPUTS AND OUTPUTS

Till Strothteicher[1], Nicolas Fezans[1], Boris Micheli[2]

[1]DLR Institute of Flight Systems
Lilienthalplatz 7, 38108 Braunschweig, Germany
till.strothteicher@dlr.de
nicolas.fezans@dlr.de

[2]DLR Institute of Aeroelasticity
Bunsenstraße 10, 37073 Goettingen, Germany
boris.micheli@dlr.de

Keywords: Damping Augmentation; Active Flutter Control; Acceleration Sensitivity; Robust Modal Control; Input/Output Blending

Abstract: A novel active flutter control, or damping augmentation, method for civil aircraft is presented. The approach leverages the link between the acceleration sensitivity of second-order systems and the damping ratio of their modes to express minimum damping constraints as frequency-domain criteria. This enables the use of modern, robust frequency-domain control design techniques, thereby taking advantage of their advanced capabilities while explicitly incorporating damping-related constraints. A similar approach was proposed in the past, using the transfer function from a (indirect) perturbation on the mode generalized acceleration to the generalized velocity of that mode. The advantage of using the acceleration sensitivity over the acceleration-to-velocity transfer function is explained. The application example, based on the DLR F-25 configuration, shows the practicality of the new approach. A structured synthesis is used, which allows comparing this new approach to the input/output blending approach by using a similar controller structure. The ability to use the method on models with a large number of modes (more than 50), many damping constraints, with robustness margin constraints, and minimizing the actuator activity (only optimization criterion) is demonstrated. The input/output blending method, even in its recently published relaxed version, does not seem suitable for such cases, whereas the proposed method is applicable for industry-scale problems. The properties and differences between the proposed method and already established approaches for damping augmentation / flutter control are summarized at the end.

1 INTRODUCTION

The drive toward lightweight structures and high–aspect-ratio wings improves aerodynamic efficiency but inherently reduces structural stiffness, leading to diminished flutter margins. Active Flutter Control (AFC) is therefore a promising enabler for such configurations. Research on AFC has a long history, dating back to the 1960s, and has been successfully demonstrated on free-flying aircraft. [1] provides a comprehensive overview. However, AFC is still not accepted for certification. In this work, the term active flutter controller is mostly used as it seems to be the most generic one, but other terms are also often used, such as *damping augmentation* or *active flutter suppression*.

One of the earliest approaches to actively damp flexible modes of a structure was to use collocate actuators and sensors and to apply a force in opposite direction of the local structural velocity, also known as Direct Velocity Feedback (DVF), to introduce an artificial local viscous damping. Such an approach was adopted and successful for the B-1 bomber to dampen the fuselage bending at the cockpit station [2, 3]. However, a DVF approach affects multiple aeroelastic modes, and can consider only one collocated actuator and sensor pair at a time. Modern civil aircraft feature several control surfaces and, possibly, a large number of sensors. Furthermore, the actuators and sensors may be at different locations.

Input/output blending for Modal Velocity Feedback (MVF) [4] addresses these challenges by isolating individual modes through linear combinations of inputs and outputs. This AFC method yields very condensed controllers and can be designed to only affect the damping of a single mode. If the damping of multiple modes is to be augmented, multiple decoupled feedback controllers are designed. The inclusion of decoupling constraints tends to yield controllers with large gains and thus with excessive actuator effort. When the considered modes have very similar mode shapes, this effect is particularly pronounced. The consequences are low robustness margins and loss of damping effectiveness when the excitations (e.g. due to turbulence), combined with these larges gains, drive the actuators to their limits. Furthermore, the number of aeroelastic modes that can be considered in the design process is limited by the number of actuators and sensors, even if the method from [5] partly relaxes this limitation. This is a major drawback for industrial applications where the number of effective actuators is small compared to the number of aeroelastic modes to consider. As it will be shown later, a significant number of aeroelastic modes also have fairly close frequencies such that a filter-based decoupling does not seem suitable.

Optimal control approaches (LQR / LQG) were investigated by, for example, NASA in the 1970s – 1990s, see e.g., [6]. The controllers yielded a damping augmentation with low actuator effort. However, one drawback of optimal control design approaches is that they offer no a-priori guarantee of robustness in case of output feedback, especially since in practice a state estimator (typically a Kalman filter in the LQG scheme) is required. The fine tuning of LQ controllers for large systems is also very difficult, such that scaling-up such approaches to industry-size problems does not seem practical.

Many of the problems or criteria in aeroservoelasticity are linked to specific modes (e.g., their damping) or can be linked to specific frequency ranges (e.g., critical gust lengths). For the latter, expressing the requirements in terms of frequency-domain specifications seems a rather obvious choice. It is however less obvious that modal-like specifications (e.g., damping objectives/constraints) can be expressed in the frequency-domain. In the case of aircraft flexible modes, as for other generalized second-order systems, a connection between the modal properties and specific transfer functions, such as the acceleration sensitivity function, can be made. This connection was already made and used in [7–9]. It was further used for space applications, such as satellites which also have a number of low-damped flexible modes [10–12].

Whilst it does not seem that the acceleration sensitivity function was already used for flutter control, a related transfer function was used in [13]. In [13], a full-order robust $\mathcal{H}_\infty$ controller synthesis process was proposed in which the damping of insufficiently damped modes is augmented by penalizing their modal velocity output in the synthesis. With this approach, the flutter speed of a small, unmanned flexible aircraft was extended from 33.3 m/s to 42.5 m/s. Compared to the acceleration sensitivity function case use in the present work, the authors of [13] use the modal velocity instead of the modal acceleration as output of the transfer function. The input of the transfer function used in [13] is also not directly a perturbation on the modal acceleration, but control surface deflections. The control surface deflections correlate well with the modal accelerations but excite several modes at once. The consequences of these differences will be detailed later in section 3.1. In the methodology proposed in the present paper, the use of the acceleration sensitivity function is preferred, but very good results can also be obtained with the approach used in [13].

Another significant difference with the work from [13] is that multi-channel/model structured synthesis (e.g., see [14, 15]) is used in this work instead of the more classical full-order $\mathcal{H}_\infty$ synthesis used in [13]. This provides significantly more flexibility in the definition of the objectives and constraints. Another major advantage is that the controller structure can be chosen with gain-scheduling and implementation constraints in mind. Thereby, the controller order can be defined a-priori such that a possible controller reduction step is not required. This, however, comes at the cost of increased computational time and the possibility of multiple local minima since the controller synthesis optimization problem is non-convex. In the authors' opinion and experience, however, the benefits of the structured synthesis outweigh the disadvantages.

Structured synthesis has been used for flutter control in [16] and [17]. In [16], the control design problem was a fairly classical mixed-sensitivity design. The approach used in [17] appears to be at the crossroads of [13] and the method proposed in this work. The focus of [17] lies, however, on the co-design structure-controller process and used a very simple model as example. Some of the templates and transfer function shown in [17, for example Fig. 5] resemble the second-order template on acceleration sensitivity (SOTAS) problems used in [7, 9]. Unlike in the previous literature using the acceleration sensitivity function, only the damping ratio is of interest in the methodology proposed in this work. This means that simple upper bounds on the $\mathcal{H}_\infty$-norm of the acceleration sensitivity function can be used: no frequency-domain template nor weighting function is needed. The damping-related criteria are optimization constraints and the only objective is to minimize the actuator activity to reduce actuator wear and to avoid, as much as possible, actuator saturation.

The paper is structured as follows. Section 2 first describes the application example considered in this paper. One of its modes becomes unstable for increasing airspeed. Section 3 describes the methods employed to stabilize that mode with minimal actuator activity while meeting stability robustness requirements. Section 4 presents the results obtained and attempts a comparison with the input/output blending concept [4, 5, 18]. Both methods have quite different properties and limitations, such that it is difficult to define a test case that allows a fair comparison. Finally, section 5 presents the conclusions and provides a condensed comparison between the method proposed in this work and the ones from [13] and [4].

2 FLUTTER CONTROL APPLICATION

The DLR-F25 is a short-medium range aircraft configuration developed as a common research benchmark, representing features typical of next-generation aircraft concepts [19]. In this study, the DLR-F25 TWIST04 configuration, described by Streitenberger & Feldwisch [20] is employed. The method proposed in the following will be used to increase to delay the flutter onset and increase the damping of the modes of this configuration.

The primary structure of the aircraft is displayed in Fig. 1a. The mass configuration considered corresponds to the aircraft delivery weight plus maximum fuel load. The aerodynamic design shape used for subsequent CFD grid generation is illustrated in Fig. 1b. To reduce computational time, pylons are omitted and the engines are modeled as a flow-through nacelle.

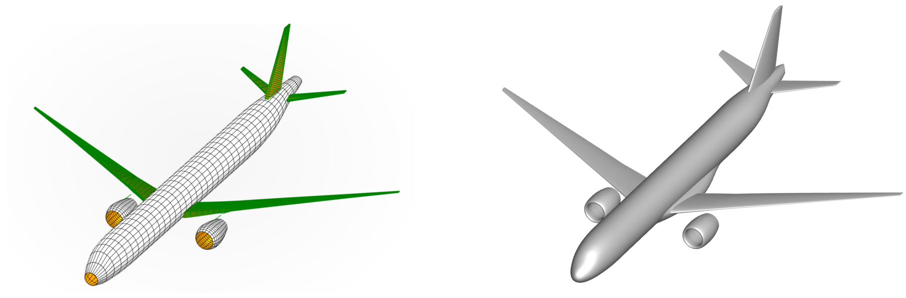

(a) Finite element model. (b) Aerodynamic shape for CFD computation.

Figure 1: DLR-F25 models.

The geometry displayed in Fig. 1b is discretized by about $2.3 \cdot 10^5$ quadrilaterals and $5.0 \cdot 10^3$ triangles. The spherical farfield has a distance of about 20 times the aircraft semi-span. The computational domain is discretized with tetrahedron and the boundary layer is resolved only on the wing wet surface using hexahedron and prism elements. The remaining walls are modeled as Euler wall boundary conditions. This wall modeling approach enabled a reduction in CFD grid size without affecting the predicted flutter behavior [21]. In total, the CFD grid comprises about $4.7 \cdot 10^6$ nodes.

The finite element model is used to compute the aircraft mass and stiffness along with the structural eigenvectors, which are then employed to generalize the aeroelastic equations of motion. A (viscous) damping of the structure of 1.5% is assumed. The eigenvectors are further interpolated using splines to the CFD surface grid via radial basis functions to permit the characterization of the Generalized Aerodynamic Forces (GAFs). In total, 46 modes were included, consisting of the roll and pitch modes along with the first 44 flexible modes. This was found to be sufficient to accurately capture the flutter behavior. The pitch mode and the first two flexible modes, which were interpolated onto the CFD surface using splines, are shown in Fig. 2.

Pitch mode. 1^{st} flexible mode. 2^{nd} flexible mode.

Figure 2: Example of structural eigenvectors splined to the CFD surface.

For the results presented in this work, the flight dynamics of the F25 were computed at a Mach number of 0.78. To compute the GAFs which describe the unsteady aerodynamic flow resulting from structural motion, control surface deflections and gust encounters, a linearized frequency-domain RANS CFD [22] was employed. The GAFs are then interpolated via the Loewner framework [23,24] to yield a rational realization that can be included in the equations of motion, thereby allowing them to be arranged in state space form. The resulting state space models are used to compute the poles of the aeroelastic system shown over varying Equivalent Air Speed (EAS) in Figure 3.

Certification requirements demand a minimum (viscous) damping of 1.5% of the aircraft's aeroelastic modes up to the dive velocity (not defined here) if 1.5% damping of the structure is assumed, see [25, AMC25.629]). The damping of the structure itself (1.5%) is marked as a dashed line. Poles with less than 22% damping, marked as a dashed-dotted line, are categorized as low-damped poles and will be constrained to a damping lower bound. Note, that the 22% damping bound for categorization is an application-specific selection. These low-damped poles are indicated with colored circles, and all other as gray circles in Fig. 3.

For the considered mass case and flight conditions, the aircraft encounters flutter at EAS $\approx$ 216 m/s. Flutter results mainly from the interaction of the second anti-symmetric wing bending (structural) mode with the anti-symmetric wing torsion (structural) mode, the latter leading to a significant engine motion. A fuselage lateral bending (structural) mode is also participating. The flutter mechanism, i.e., aeroelastic mode, is displayed in Fig. 4.

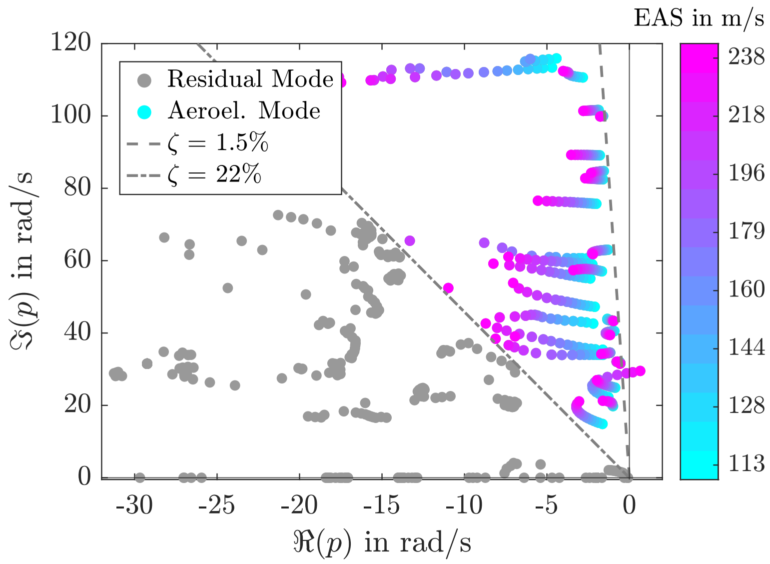

Figure 3: Map of the F25 models aeroelastic poles over varying Equivalent Air Speed (EAS).

The damping of this mode is later artificially increased with the AFC. The aircraft is equipped with four multi-functional flaps on the main wing and an elevator at the horizontal tailplane that can be used to mitigate the flutter behavior. The ailerons on the left and right wing-half, noted $\delta^{\mathrm{L}}_{\mathrm{a},\square}$ and $\delta^{\mathrm{R}}_{\mathrm{a},\square}$ respectively, are mixed to define symmetric ($\delta^{\mathrm{sym}}_{\mathrm{a},\square}$) and anti-symmetric ($\delta^{\mathrm{asym}}_{\mathrm{a},\square}$) deflections. The elevators are only deflected symmetrically. The rudder is also defined in the aerodynamic mesh, but not used. The aircraft is instrumented with several uniaxial accelerometers that are positioned throughout the airframe to measure the local vertical acceleration. These signals are available for feedback purposes.

Figure 5 shows both locations and notations of the control surfaces and sensors considered. All trailing edge sensors are labeled for the wing and the horizontal stabilizer ($a^{\square,\mathrm{TE}}_{\mathrm{z},\square}$). However, the respective leading edge sensor ($a^{\square,\mathrm{LE}}_{\mathrm{z},\square}$) is also considered to measure the local bending and torsion acceleration. The location of the leading-edge sensors is illustrated using the outermost sensor on the left wing $a^{\mathrm{L,LE}}_{\mathrm{z},7}$ as an example.

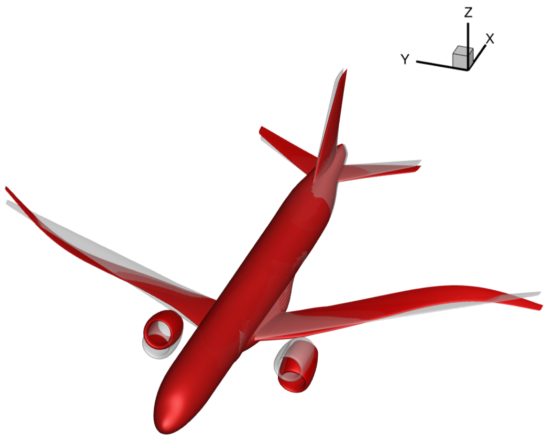

Figure 4: Flutter mechanism of the DLR-F25 at Mach=0.78 for the considered mass case.

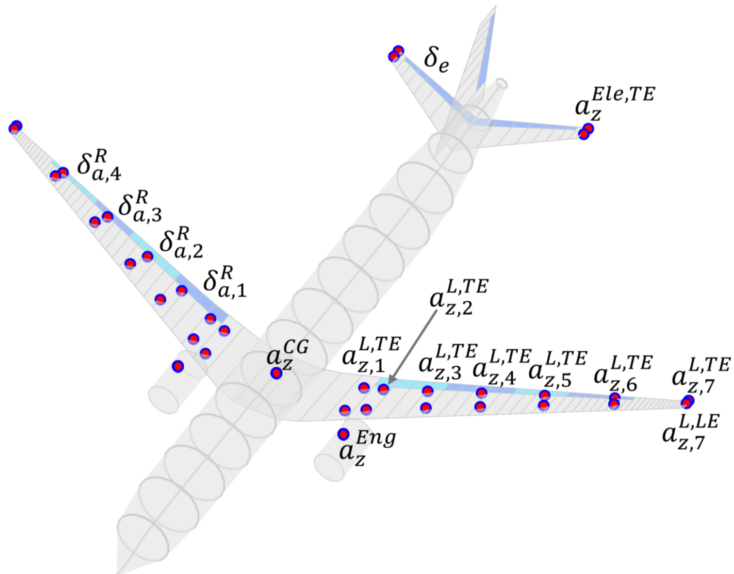

Figure 5: Sensor and control surface positions throughout the airframe.

The actuators to drive the control surfaces are modeled as second-order systems with a natural frequency of $\omega_\mathrm{n} = 43\,\mathrm{rad/s}$ and a relative damping of $\zeta = 0.68$. The actuator and sensor dynamics are coupled with the aeroelastic equations of motion to provide the state space realization of the aeroservoelastic plant to be controlled. The final state space models comprise 789 states, which are reduced to 130 states for controller design using a combination of balanced and modal reduction techniques. The flap deflections are commanded via the previously defined symmetrical and anti-symmetrical commands. Thus the following commanded flap deflections are available as an input:

$$\mathbf{u} = [\delta_\mathrm{e}, \delta^\mathrm{sym}_\mathrm{a,1,cmd}, \delta^\mathrm{sym}_\mathrm{a,2,cmd}, \delta^\mathrm{sym}_\mathrm{a,3,cmd}, \delta^\mathrm{sym}_\mathrm{a,4,cmd}, \delta^\mathrm{asym}_\mathrm{a,1,cmd}, \delta^\mathrm{asym}_\mathrm{a,2,cmd}, \delta^\mathrm{asym}_\mathrm{a,3,cmd}, \delta^\mathrm{asym}_\mathrm{a,4,cmd}] \,. \tag{1}$$

Finally, the trailing and leading edge sensors are mixed at the respective wing and horizontal tailplane sections to measure the local symmetric bending ($a^\mathrm{sB}_{\mathrm{z},\square}$), the local symmetric torsion ($a^\mathrm{sT}_{\mathrm{z},\square}$), the local anti-symmetric bending ($a^\mathrm{aB}_{\mathrm{z},\square}$), and the local anti-symmetric torsion ($a^\mathrm{aT}_{\mathrm{z},\square}$). The sensors on the engine are mixed to measure the symmetric bending $a^\mathrm{sB}_\mathrm{z,Eng}$ and anti-symmetric bending $a^\mathrm{aB}_\mathrm{z,Eng}$ only, as there is only one sensor available instead of a sensor pair. In total there are 34 mixed measurement outputs $\mathbf{y}$ (not shown here for conciseness, see later in Fig. 13).

With this sensor and actuator setup, the damping of the flutter mode can be increased. The methods employed for designing suitable controllers are presented in the next section.

3 METHODS

This section presents a new method for flutter controller design. The first subsection, 3.1, outlines a way to link the damping of weakly damped modes of generalized second-order systems (which the isolated aeroelastic modes of an aeroelastic systems can usually be considered to be) to a frequency-domain transfer function norm, and compares it to a relatively similar approach used in [13]. In both cases (approaches from [13] and from this work), a transformation of the linear time-invariant state-space model (LTI SSM) is required to define the transfer functions whose norm is used to define the mode-damping objectives / constraints. Said transformation is outlined later in subsection 3.2.3. It allows the LTI SSM to be extended with new inputs and outputs of the transfer function that are related to the damping of the weakly damped mode. These inputs and outputs are then employed in the controller design, presented in subsection 3.2, to impose mode-specific damping-lower-bound constraints (subsection 3.2.3).

3.1 Quantifying Damping in the Frequency Domain

A LTI SSM in real Jordan normal form [26] describing an aeroelastic system with n_u control inputs, n_y sensor outputs, and n_x states is defined as

$$\tilde{\mathbf{G}} : \left[\begin{array}{c} \dot{\tilde{\mathbf{x}}} \\ \hline \mathbf{y} \end{array}\right] = \left[\begin{array}{ccc|c} \tilde{\mathbf{A}}_1 & & \mathbf{0} & \tilde{\mathbf{B}}_1 \\ & \ddots & & \vdots \\ \mathbf{0} & & \tilde{\mathbf{A}}_{\mathrm{n_i}} & \tilde{\mathbf{B}}_{\mathrm{n_i}} \\ \hline \tilde{\mathbf{C}}_1 & \cdots & \tilde{\mathbf{C}}_{\mathrm{n_i}} & \mathbf{0} \end{array}\right] \left[\begin{array}{c} \tilde{\mathbf{x}} \\ \hline \mathbf{u} \end{array}\right] . \tag{2}$$

The system $\tilde{\mathbf{G}}$ consists of n_i oscillating modes. Modes with real poles (not oscillating) are omitted here as they are not of interest for damping constraints. Each of the aeroelastic modes $\mathbf{M}_\mathrm{i}$ ($i \in [\![1, n_\mathrm{i}]\!]$) is thus defined by a second-order LTI SSM

$$\mathbf{M}_\mathrm{i} : \left[\begin{array}{c} \dot{\eta}_\mathrm{i} \\ \ddot{\eta}_\mathrm{i} \\ \hline \mathbf{y}_\mathrm{i} \end{array}\right] = \left[\begin{array}{c|c} \mathbf{A}_\mathrm{i} & \mathbf{B}_\mathrm{i} \\ \hline \mathbf{C}_\mathrm{i} & \mathbf{0} \end{array}\right] \left[\begin{array}{c} \eta_\mathrm{i} \\ \dot{\eta}_\mathrm{i} \\ \hline \mathbf{u} \end{array}\right] = \left[\begin{array}{cc|c} 0 & 1 & \mathbf{b}_{1,\mathrm{i}}^\mathrm{T} \\ -\omega_{\mathrm{n,i}}^2 & -2\,\zeta_\mathrm{i}\,\omega_{\mathrm{n,i}} & \mathbf{b}_{2,\mathrm{i}}^\mathrm{T} \\ \hline \mathbf{c}_{1,\mathrm{i}} & \mathbf{c}_{2,\mathrm{i}} & \mathbf{0} \end{array}\right] \left[\begin{array}{c} \eta_\mathrm{i} \\ \dot{\eta}_\mathrm{i} \\ \hline \mathbf{u} \end{array}\right] \tag{3}$$

based on its modal deflection, velocity and acceleration $\eta_\mathrm{i}, \dot{\eta}_\mathrm{i}, \ddot{\eta}_\mathrm{i}$, relative damping ζ_i, and natural angular frequency $\omega_{\mathrm{n,i}}$. The state transformation used to achieve this realization is described in subsection 3.2.3. The relative damping of each mode ζ_i is directly related to the $\mathcal{H}_\infty$ norm of the transfer function from a modal acceleration disturbance ${\ddot{\eta}_\mathrm{i}}^\mathrm{in}$ to the modal velocity ${\dot{\eta}_\mathrm{i}}^\mathrm{out}$ (cf. [13])

$$\left\| {\ddot{\eta}_\mathrm{i}}^\mathrm{in} \to {\dot{\eta}_\mathrm{i}}^\mathrm{out} \right\|_\infty = \left\| \frac{s}{s^2 + 2\,\zeta_\mathrm{i}\,\omega_{\mathrm{n,i}}\,s + \omega_{\mathrm{n,i}}^2} \right\|_\infty = \frac{1}{2\,\zeta_\mathrm{i}\,\omega_{\mathrm{n,i}}} \tag{4}$$

and to the $\mathcal{H}_\infty$ norm of the acceleration sensitivity (cf. [7, 8, 11]) transfer function ${\ddot{\eta}_\mathrm{i}}^\mathrm{in} \to {\ddot{\eta}_\mathrm{i}}^\mathrm{out}$

$$\left\| {\ddot{\eta}_\mathrm{i}}^\mathrm{in} \to {\ddot{\eta}_\mathrm{i}}^\mathrm{out} \right\|_\infty = \left\| \frac{s^2}{s^2 + 2\,\zeta_\mathrm{i}\,\omega_{\mathrm{n,i}}\,s + \omega_{\mathrm{n,i}}^2} \right\|_\infty = \begin{cases} \frac{1}{2\,\zeta_\mathrm{i}\sqrt{1-\zeta_\mathrm{i}^2}} & \text{if } \zeta_\mathrm{i} \le \frac{1}{\sqrt{2}} \\ 1 & \text{otherwise} \end{cases} . \tag{5}$$

Figure 6a and 6b show the relations between the $\mathcal{H}_\infty$ norm of the acceleration-to-velocity / acceleration sensitivity, and the damping (as well as natural angular frequency) of an oscillating mode. The fact that the link between damping ratio and the $\mathcal{H}_\infty$ norm of the transfer from modal acceleration to modal velocity depends on the modes natural angular frequency can well be seen in Fig. 6a. This dependency is not present with the acceleration sensitivity function, cf. Fig. 6b.

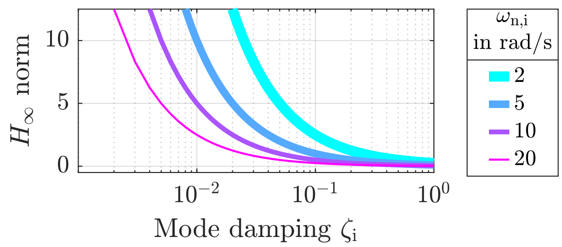

(a) Accel.-to-velocity sensitivity ($\ddot{\eta}_i{}^{in} \rightarrow \dot{\eta}_i{}^{out}$)

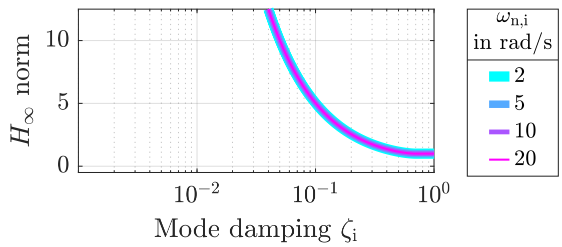

(b) Acceleration sensitivity ($\ddot{\eta}_i{}^{in} \rightarrow \ddot{\eta}_i{}^{out}$)

Figure 6: $\mathcal{H}_\infty$ norm of Acceleration-to-Velocity and Acceleration Sensitivity over mode damping of a generic second order system.

Indeed, the $\mathcal{H}_\infty$-norm of the acceleration-to-velocity transfer function rather correlated with the real part of the modes eigenvalue. This is illustrated in Fig. 7a where the $\mathcal{H}_\infty$-norm is represented as contour levels for a second-order system. The real part of the eigenvalue correlates strongly with the relative damping for very low damped modes for any given mode frequency. However, the relationship is not constant for different mode frequencies and a slight change in frequency can occur with the addition of the flutter controller. The fact that the contour levels of $\mathcal{H}_\infty$-norm for the (unweighted) acceleration sensitivity of a second-order system correspond to the iso-damping lines is illustrated in Fig. 7b.

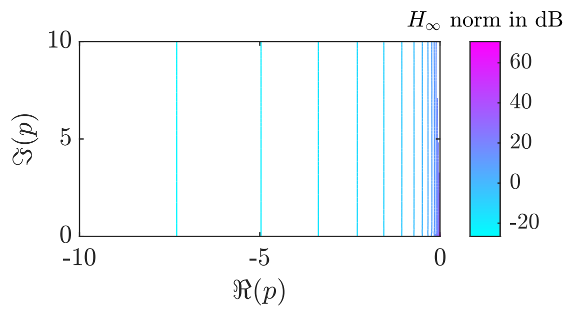

(a) Accel.-to-velocity sensitivity

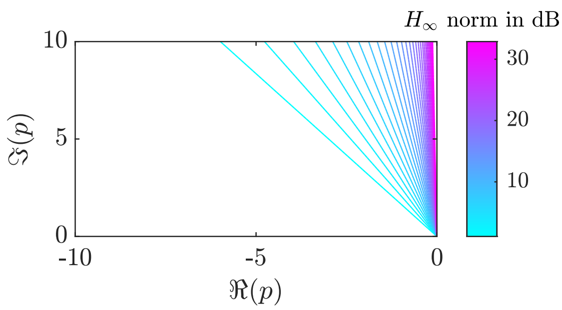

(b) Acceleration sensitivity

Figure 7: $\mathcal{H}_\infty$ norm of Acceleration-to-Velocity and Acceleration Sensitivity depending on the pole position of a generic second order system. Lines are of constant $\mathcal{H}_\infty$ norm.

This difference is the main motivation for using the acceleration sensitivity to implement minimum damping constraints in the proposed method. This is a pure constraint on the mode damping[1] and no correction with the mode frequency is needed.

[1]Assuming that the closed-loop transfer function is also in the shape of a second order high-pass filter.

3.2 Multi-Objective Control Design

The MATLAB `systune` framework [27] is used in this paper for solving the controller synthesis problem. Multiple control objectives can be defined based on the $\mathcal{H}_2/\mathcal{H}_\infty$ norms of the plants transfer functions. Furthermore, the framework allows for structured control law synthesis. That is, the control designer defines a closed-loop structure with fixed-order control elements and the tunable elements are then optimized to meet frequency-domain tuning requirements. The closed-loop synthesis setup is shown in Fig. 8, illustrating the control architecture used for defining the tuning requirements. For now, a generic controller $\mathbf{K}$ is employed to artificially increase the damping of insufficiently damped aeroelastic modes of the plant $\mathbf{G}$. This section focuses on the tuning objectives and constraints. The selected controller structure is presented in subsection 3.3.

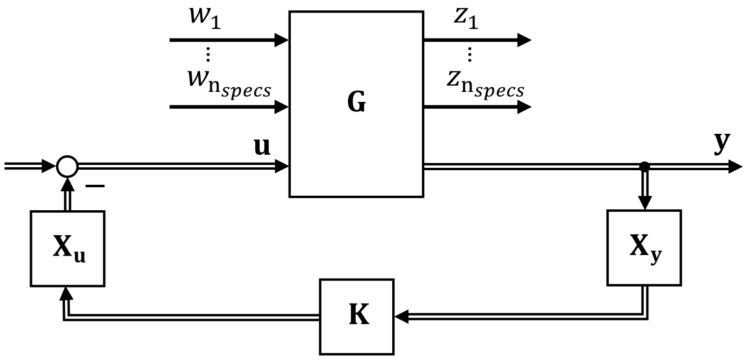

Figure 8: Closed-loop active flutter control system for automated tuning.

The `Analysis Points` $\mathbf{X_u}$ and $\mathbf{X_y}$, cf. Fig. 8, are employed during the tuning process to impose closed-loop stability robustness margins. `Analysis Points` are used as inputs and outputs at the given location in the closed-loop, without actually modifying the model. In the signal flow direction, an `Analysis Point` first outputs the signal and then allows an input to be added.

A series of exogenous inputs w_i ($i \in [\![1, n_{\text{specs}}]\!]$) and outputs z_i ($i \in [\![1, n_{\text{specs}}]\!]$) can be defined/added to the tuning problem. The corresponding transfer functions $T_{w_i \to z_i}$ ($i \in [\![1, n_{\text{specs}}]\!]$) are then used to specify control design objectives (soft requirements) or constraints (hard requirements). These tuning requirements are defined using either the $\mathcal{H}_2$ or the $\mathcal{H}_\infty$ norm[2] of each of these (weighted or unweighted) transfer functions. For example, to minimize the controller gain an $\mathcal{H}_2$ criterion on the actuator activity is defined as the objective, whereas the damping lower bound constraints are $\mathcal{H}_\infty$ constraints on the acceleration sensitivity function of the considered modes.

Additional hard requirements are applied on the stability robustness (5 dB|40 deg multi-loop disk margin [29] on all inputs or all outputs simultaneously) and on the closed-loop damping of the aeroelastic modes. The lower bound on the closed-loop damping is the maximum of the viscous structural and open-loop damping $\max\{\zeta_{\text{FE,i}}, \zeta_{\text{OL,i}}\}$ such that the damping of the residual modes is maintained while the damping of the flutter mode is increased.

In total there are three types of tuning requirements for the flutter controller, which are summarized in Tab. 1 and explained in the following. The two first are defined once for the whole system, whereas the third one is repeated for each of the low-damped modes.

[2] Interpretations and more information on the $\mathcal{H}_2/\mathcal{H}_\infty$ norms can be found in [28]

Table 1: Controller tuning goals

Number	Aim	Type	Location	Target
		Cost function (`systune` soft requirement)		
#1	Minimize Actuator Effort	$\mathcal{H}_2$	$\mathbf{T}_{\mathbf{d}\rightarrow\dot{\boldsymbol{\delta}}_{\text{act}}}$	0
		Constraints (`systune` hard requirements)		
#2	Feedback Stability Margin	Disk Margin	$\mathbf{X}_\mathbf{u}$, $\mathbf{X}_\mathbf{y}$ (separately)	$\geq 5\,\text{dB}\vert 40\,\text{deg}$
#3	Damping Lower Bound (for each aeroelastic mode)	$\mathcal{H}_\infty$	$T_{\ddot{\eta}_\text{i}{}^\text{in}\rightarrow\ddot{\eta}_\text{i}{}^\text{out}}$	$\leq \dfrac{1}{2\zeta_{\text{LB,i}}\sqrt{1-\zeta_{\text{LB,i}}^2}}$, $\zeta_{\text{LB,i}} = \max\{\zeta_{\text{FE,i}}, \zeta_{\text{OL,i}}\}$

3.2.1 Actuator Effort

Active flutter control systems must avoid excessive use of the actuators since control surface actuators are subject to nonlinear constraints in position, velocity, and acceleration. These physical limits imply that excessive control demands can drive actuators into saturation, where the commanded response can no longer be tracked. This may lead to a significant degradation in closed-loop stability and performance. In the context of flutter control, this risk is pronounced because controllers designed to stabilize specific structural modes are inherently sensitive to mode-aligned disturbances. For example, if the flutter controller is designed to increase the damping of a symmetric wing bending mode, vertical turbulence may induce high-frequency and high-amplitude control demands, potentially causing actuator rate saturation. Excessive actuator usage may further cause a series of undesired effects an especially increased actuator wear which results in higher maintenance cost. It would also lead to increased energy consumption and some drag increase.

To address these concerns, the actuator effort is minimized by defining it as the cost function. The actuator effort can be quantified by a transfer function from an excitation of the flutter controller to the rates of all actuators. As the flutter controller is designed to increase the damping of insufficiently damped aeroelastic modes, the choice of inputs depends on the shape of these modes. For the application case considered, where the flutter mode is anti-symmetric, all possible anti-symmetric aileron deflection commands are used as a surrogate excitation (exogenous input w_1). The vector $\mathbf{d}$ of anti-symmetric aileron deflection commands is:

$$\mathbf{d} = \begin{bmatrix} \delta_{\text{a,1,cmd}}^{\text{asym}} & \delta_{\text{a,2,cmd}}^{\text{asym}} & \delta_{\text{a,3,cmd}}^{\text{asym}} & \delta_{\text{a,4,cmd}}^{\text{asym}} \end{bmatrix}^T . \tag{6}$$

The corresponding exogenous output z_1 is defined a the vector of actuator deflection rates $\dot{\boldsymbol{\delta}}_{\text{act}}$:

$$\dot{\boldsymbol{\delta}}_{\text{act}} = \left[\dot{\delta}_\text{e},\ \dot{\delta}_{\text{a},1}^\text{L},\ \dot{\delta}_{\text{a},2}^\text{L},\ \dot{\delta}_{\text{a},3}^\text{L},\ \dot{\delta}_{\text{a},4}^\text{L},\ \dot{\delta}_{\text{a},1}^\text{R},\ \dot{\delta}_{\text{a},2}^\text{R},\ \dot{\delta}_{\text{a},3}^\text{R},\ \dot{\delta}_{\text{a},4}^\text{R}\right]^\text{T} . \tag{7}$$

The objective function is therefore: $\min\limits_{\mathbf{K}} ||\mathbf{T}_{\mathbf{d}\rightarrow\dot{\boldsymbol{\delta}}_{\text{act}}}(s)||_2$.

3.2.2 Stability margins

Stability margin requirements are applied to provide robustness against system uncertainties. Classical stability margins are measures of variations in gain or phase that can be tolerated whilst maintaining closed-loop stability [29]. Classical gain and phase margins $GM|PM$ of at least 5 dB|40 deg are specified at the `Analysis Points` $\mathbf{X_u}$ and $\mathbf{X_y}$ in Fig. 8. To further ensure robustness against simultaneous variations in gain and phase, disk margins for simultaneous variation of all inputs or all outputs are employed in the tuning process instead of classical margins for single loops.

The classical margin specification is translated to an unskewed disk with radius

$$\alpha = 2\max\left\{(GM-1)/(GM+1), \tan(PM/2)\right\} \ , \tag{8}$$

which serves as a lower bound on the disk margin of the corresponding multi-input multi-output (MIMO) loop. The latter is defined as $1/\left(||\mathbf{D}^{-1}(\mathbf{I}-\mathbf{L}(s))(\mathbf{I}+\mathbf{L}(s))^{-1}\mathbf{D}||_{\infty}\right)$, where $\mathbf{L}(s)$ denotes the open-loop transfer function (recall the `Analysis Point` description), and $\mathbf{D}(s)$ denotes a static diagonal scaling matrix which compensates for differences in signal magnitudes [27, 29]. These stability margin requirements are realized using the `tuningGoal.Margin` requirement (feature of the `systune` framework).

3.2.3 Damping Lower Bound

The closed-loop damping of each of the n_{ld} low-damped mode is constrained to a lower bound $\zeta_{\mathrm{LB,i}}$ using the $\mathcal{H}_{\infty}$ norm of the acceleration sensitivity, cf. subsection 3.1. The damping lower bound constraint is defined either by the damping of the structure itself or by the mode's open-loop damping, whichever is greater:

$$\forall i \in [\![1, n_{\mathrm{ld}}]\!], \zeta_{\mathrm{LB,i}} = \max\left(\,\zeta_{\mathrm{FE,i}},\, \zeta_{\mathrm{OL,i}}\,\right) \ . \tag{9}$$

This yields the $\mathcal{H}_{\infty}$ norm constraints:

$$\forall i \in [\![1, n_{\mathrm{ld}}]\!], \ \ ||T_{\ddot{\eta}_{\mathrm{i}}{}^{\mathrm{in}} \to \dot{\eta}_{\mathrm{i}}{}^{\mathrm{out}}}||_{\infty} \leq \frac{1}{2\,\zeta_{\mathrm{LB,i}}\sqrt{1-\zeta_{\mathrm{LB,i}}^{2}}} \ . \tag{10}$$

Note that, due to the feedback controller being able to introduce cross-coupling between modes, the employed transfer functions could no longer be equivalent to a second-order system, which may lead to a (limited) violation of the damping lower bound constraint. This should be checked afterwards and possibly corrected with slight tightening of the constraint.

The input and output to the acceleration sensitivity function (respectively acceleration-to-velocity transfer function) of an aeroelastic mode may not be available for a given LTI SSM. In order to add these inputs and outputs, the same state transformation as for the Input/Ouput Blending method [4] is applied (largely the same as in [5]). The system $\tilde{\mathbf{G}}$ is in real Jordan normal form, recall Eq. 2. This state space representation is obtained through a state transformation based on the eigenvectors of the system, see [4, 26]. The system $\tilde{\mathbf{G}}$ consists of n_{i} conjugate complex pole pairs $p_{\mathrm{i}} = \Re(p_{\mathrm{i}}) \pm \sqrt{-1}\Im(p_{\mathrm{i}})$, with $i \in [\![1, n_{\mathrm{i}}]\!]$. The response of each individual mode is hence described through

$$\tilde{\mathbf{M}}_\mathrm{i}:\left[\begin{array}{c}\dot{\tilde{\mathbf{x}}}_\mathrm{i}\\\hline \mathbf{y}_\mathrm{i}\end{array}\right]=\left[\begin{array}{c|c}\tilde{\mathbf{A}}_\mathrm{i}&\tilde{\mathbf{B}}_\mathrm{i}\\\hline \tilde{\mathbf{C}}_\mathrm{i}&\mathbf{0}\end{array}\right]\left[\begin{array}{c}\tilde{\mathbf{x}}_\mathrm{i}\\\hline \mathbf{u}\end{array}\right]=\left[\begin{array}{cc|c}\Re(p_\mathrm{i})&\Im(p_\mathrm{i})&\Re(\tilde{\mathbf{b}}_\mathrm{i})^\mathrm{T}\\-\Im(p_\mathrm{i})&\Re(p_\mathrm{i})&-\Im(\tilde{\mathbf{b}}_\mathrm{i})^\mathrm{T}\\\hline \Re(\tilde{\mathbf{c}}_\mathrm{i})&\Im(\tilde{\mathbf{c}}_\mathrm{i})&\mathbf{0}\end{array}\right]\left[\begin{array}{c}\tilde{\mathbf{x}}_\mathrm{i}\\\hline \mathbf{u}\end{array}\right]. \tag{11}$$

While the states of these second-order systems have no intuitive physical meaning they can be transformed into the physical realization characterized by the relative damping $\zeta_\mathrm{i}=-\Re(p_\mathrm{i})/\omega_{\mathrm{n,i}}$, and natural angular frequency $\omega_{\mathrm{n,i}}=|p_\mathrm{i}|$

$$\mathbf{M}_\mathrm{i}:\left[\begin{array}{c}\dot{\eta}_\mathrm{i}\\\ddot{\eta}_\mathrm{i}\\\hline \mathbf{y}_\mathrm{i}\end{array}\right]=\left[\begin{array}{c|c}\mathbf{A}_\mathrm{i}&\mathbf{B}_\mathrm{i}\\\hline \mathbf{C}_\mathrm{i}&\mathbf{0}\end{array}\right]\left[\begin{array}{c}\eta_\mathrm{i}\\\dot{\eta}_\mathrm{i}\\\hline \mathbf{u}\end{array}\right]=\left[\begin{array}{cc|c}0&1&\mathbf{b}_{1,\mathrm{i}}^\mathrm{T}\\-\omega_{\mathrm{n,i}}^2&-2\,\zeta_\mathrm{i}\,\omega_{\mathrm{n,i}}&\mathbf{b}_{2,\mathrm{i}}^\mathrm{T}\\\hline \mathbf{c}_{1,\mathrm{i}}&\mathbf{c}_{2,\mathrm{i}}&\mathbf{0}\end{array}\right]\left[\begin{array}{c}\eta_\mathrm{i}\\\dot{\eta}_\mathrm{i}\\\hline \mathbf{u}\end{array}\right] \tag{12}$$

through a similarity transformation $\tilde{\mathbf{x}}_\mathrm{i}=\tilde{\mathbf{T}}_\mathrm{i}\,\mathbf{x}_\mathrm{i}=\tilde{\mathbf{T}}_\mathrm{i}\,[\eta_\mathrm{i}\quad\dot{\eta}_\mathrm{i}]^\mathrm{T}$. The transformation matrices suitable for this purpose are given by

$$\tilde{\mathbf{T}}_\mathrm{i}(\phi)=\begin{bmatrix}\Re(p_\mathrm{i})\sin(\phi)-\Im(p_\mathrm{i})\cos(\phi)&-\sin(\phi)\\\Im(p_\mathrm{i})\sin(\phi)+\Re(p_\mathrm{i})\cos(\phi)&-\cos(\phi)\end{bmatrix} \tag{13}$$

which is parametrized over the state transformation angle $\phi\in\mathbb{R}$ [26], cf. also [4]. All possible similarity transformations yield a system matrix which is unique $\mathbf{A}_\mathrm{i}=\tilde{\mathbf{T}}_\mathrm{i}^{-1}(\phi)\tilde{\mathbf{A}}_\mathrm{i}\tilde{\mathbf{T}}_\mathrm{i}(\phi)$ for all ϕ. However, the input and output matrices following from this similarity transformation

$$\begin{bmatrix}\mathbf{b}_{1,\mathrm{i}}^\mathrm{T}(\phi)\\\mathbf{b}_{2,\mathrm{i}}^\mathrm{T}(\phi)\end{bmatrix}=\tilde{\mathbf{T}}_\mathrm{i}^{-1}(\phi)\begin{bmatrix}\Re(\tilde{\mathbf{b}}_\mathrm{i})^\mathrm{T}\\-\Im(\tilde{\mathbf{b}}_\mathrm{i})^\mathrm{T}\end{bmatrix},\quad\begin{bmatrix}\mathbf{c}_{1,\mathrm{i}}(\phi)&\mathbf{c}_{2,\mathrm{i}}(\phi)\end{bmatrix}=\begin{bmatrix}\Re(\tilde{\mathbf{c}}_\mathrm{i})&\Im(\tilde{\mathbf{c}}_\mathrm{i})\end{bmatrix}\tilde{\mathbf{T}}_\mathrm{i}(\phi) \tag{14}$$

are not unique, but depend on ϕ. Note that the similarity transformation matrix is periodic $\forall\,k\in\mathbb{Z},\ \tilde{\mathbf{T}}_\mathrm{i}(\phi)=\tilde{\mathbf{T}}_\mathrm{i}(\phi+k\pi)$. The state transformation is carried out for each mode with the optimal state transformation angle $\phi^\star$

$$\phi^\star=\underset{\phi}{\mathrm{argmax}}\Big(||\mathbf{c}_{2,\mathrm{i}}(\phi)\,\mathbf{b}_{2,\mathrm{i}}^\mathrm{T}(\phi)||_2(2\sqrt{\omega_n\zeta}\mathbf{M}_\mathrm{i})^{-1}\Big)\ . \tag{15}$$

This is the state transformation with the largest blending efficiency (refer to [4] for more information). Lastly, the inputs and outputs to the acceleration sensitivity (${\ddot{\eta}_\mathrm{i}}^{\mathrm{in}}$ and ${\ddot{\eta}_\mathrm{i}}^{\mathrm{out}}$) are added to the LTI SSM for each aeroelastic mode, recall Eq. 12, by adding the corresponding columns and rows to the LTI SSM: The B-Matrix of each mode is extended by $[0\ 1]^\mathrm{T}$, thereby adding an input to the generalized acceleration of each mode $\ddot{\eta}_\mathrm{i}^{\mathrm{in}}$. The C-Matrix is extended by the second row of the modes $\mathbf{A}_\mathrm{i}$ matrix, which yields new outputs of the generalized acceleration of each mode $\ddot{\eta}_\mathrm{i}^{\mathrm{out}}$ (same process as shown already in [9] and subsequent work using the acceleration sensitivity function). This leads to the structure of Eq. 16), when considering multiple modes at once. For simplificity, in this equation, the acceleration sensitivity function is defined for all modes in this equation. In practice, if the damping lower bounds are only defined for a subset of the modes, not all rows and columns will be needed. Note that providing $\dot{\eta}_{\mathrm{i}}^{\mathrm{out}}$ as an output is very straightforward as it is also a state (simply add the whole $\mathbf{A}_{\mathrm{i}}$ matrix to the C-Matrix)

$$
\left[\begin{array}{c}
\dot{\eta}_1 \\ \ddot{\eta}_1 \\ \vdots \\ \dot{\eta}_{\mathrm{n_i}} \\ \ddot{\eta}_{\mathrm{n_i}} \\ \hline \ddot{\eta}_1^{\mathrm{out}} \\ \vdots \\ \ddot{\eta}_{\mathrm{n_i}}^{\mathrm{out}} \\ \hline \mathbf{y}
\end{array}\right]
=
\left[\begin{array}{ccccc|c|c}
0 & 1 & & 0 & 0 & 0 \dots 0 & \mathbf{b}_{1,1}^{\mathrm{T}} \\
-\omega_{\mathrm{n},1}^2 & -2\zeta_1\omega_{\mathrm{n},1} & & 0 & 0 & 1 \dots 0 & \mathbf{b}_{2,1}^{\mathrm{T}} \\
\vdots & \vdots & \ddots & \vdots & \vdots & \ddots & \vdots \\
0 & 0 & & 0 & 1 & 0 \dots 0 & \mathbf{b}_{1,\mathrm{n_i}}^{\mathrm{T}} \\
0 & 0 & & -\omega_{\mathrm{n},\mathrm{n_i}}^2 & -2\zeta_{\mathrm{n_i}}\omega_{\mathrm{n},\mathrm{n_i}} & 0 \dots 1 & \mathbf{b}_{2,\mathrm{n_i}}^{\mathrm{T}} \\ \hline
-\omega_{\mathrm{n},1}^2 & -2\zeta_1\omega_{\mathrm{n},1} & & 0 & 0 & & \\
\vdots & \vdots & \ddots & \vdots & \vdots & \mathbf{I}_{n_i \times n_i} & \mathbf{0}_{n_i \times n_u} \\
0 & 0 & & -\omega_{\mathrm{n},\mathrm{n_i}}^2 & -2\zeta_{\mathrm{n_i}}\omega_{\mathrm{n},\mathrm{n_i}} & & \\ \hline
\mathbf{c}_{1,1} & \mathbf{c}_{2,1} & \dots & \mathbf{c}_{1,\mathrm{n_i}} & \mathbf{c}_{2,\mathrm{n_i}} & \mathbf{0}_{n_y \times n_i} & \mathbf{0}_{n_y \times n_u}
\end{array}\right]
\left[\begin{array}{c}
\eta_1 \\ \dot{\eta}_1 \\ \vdots \\ \eta_{\mathrm{n_i}} \\ \dot{\eta}_{\mathrm{n_i}} \\ \hline \ddot{\eta}_1^{\mathrm{in}} \\ \vdots \\ \ddot{\eta}_{\mathrm{n_i}}^{\mathrm{in}} \\ \hline \mathbf{u}
\end{array}\right]
\tag{16}
$$

3.3 Controller Structure

The controller structure is based on that of the input/output blending approach, see [4], which will make it easier to compare the two methods. Any other feedback controller structure could be used as well. The controller structure from [4] is a proportional feedback controller which linearly combines the inputs and outputs, yielding just $n_{\mathrm{u}} + n_{\mathrm{y}}$ controller parameters. The controller from [4] consists of unit-length input and output blending vectors, and a single-input single-output (SISO) feedback gain λ. The feedback gain is replaced in this work by a tunable dynamic SISO controller $\mathbf{K}_{\mathrm{dyn}}$ to assign the controller a bandwidth, and to expand the design flexibility during optimization. $\mathbf{K}_{\mathrm{dyn}}$ consists of a gain λ, a non-tunable band-pass filter $F_{\mathrm{BPF}}(s)$,

$$
F_{\mathrm{BPF}}(s) = \frac{s^2}{s^2 + \zeta_{\mathrm{HP}}\omega_{\mathrm{HP}}s + \omega_{\mathrm{HP}}^2} \cdot \frac{\omega_{\mathrm{LP}}^2}{s^2 + \zeta_{\mathrm{LP}}\omega_{\mathrm{LP}}s + \omega_{\mathrm{LP}}^2} \,, \tag{17}
$$

and a tunable SISO state space system $F_{\mathrm{tune}}(s)$ with six tunable states $n_{\mathrm{x,tune}} = 6$. This structure was chosen to ensure a band-pass behavior of the flutter controller. Figure 9 shows the structure of the flutter control system. The input/output blending vectors, $\mathbf{k}_{\mathrm{u}}$ and $\mathbf{k}_{\mathrm{y}}$ respectively, are

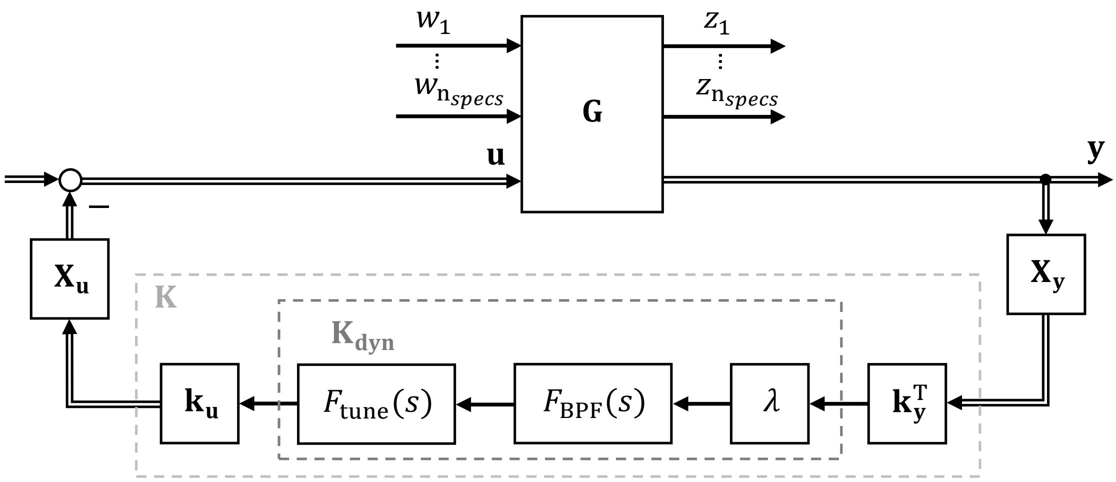

Figure 9: Closed-loop active flutter control system for automated tuning. Controller structure based on Input/Output blending controller [4], extended with dynamic (tunable) filters.

tunable vectors of appropriate size. The blending vectors as well as the dynamic elements of

$\mathbf{K}_{\mathrm{dyn}}$ are normalized to a resonance magnitude of 0 dB after the controller synthesis, such that the feedback gain is defined by λ at the resonance frequency of $\mathbf{K}_{\mathrm{dyn}}$. The band-pass filter damping constants ζ_{HP} and ζ_{LP} are set to $1/\sqrt{2}$ for all controllers presented in the next section.

4 TESTS AND RESULTS ON APPLICATION EXAMPLE

The presented methods are used to synthesize a structured $\mathcal{H}_2/\mathcal{H}_\infty$ controller for the exemplary aircraft introduced in section 2 with the controller structure described in subsection 3.3. The high-pass bandwidth is set to $\omega_{\mathrm{HP}} = 10\,\mathrm{rad/s}$ and the low-pass bandwidth to $\omega_{\mathrm{LP}} = 80\,\mathrm{rad/s}$ such that the filter has a large magnitude at the flutter modes frequency. The tunable filter can alter the dynamic behavior though if deemed beneficial for meeting the tuning requirements.

Furthermore, to demonstrate the advantages of this approach, the resulting controller is compared to two benchmark controllers designed with the Input/Output Blending Method for Modal Velocity Feedback from [4] (extended by a band-pass filter). Their design is outlined in the following subsection, 4.1, and more detailed information on the band-pass filter for the benchmark controllers can be found at the very end of this section in subsection 4.3.

4.1 Benchmark Controllers

The benchmark controllers also have the structure of Fig. 9. The input and output blending vectors, $\mathbf{k}_{\mathrm{u}}$ and $\mathbf{k}_{\mathrm{y}}$ respectively, are optimized for maximum observability / controllability of the primary mode. The primary mode is the one whose damping is artificially increased by the feedback controller. For the given example, the primary mode is the flutter mode. The feedback gain is selected such that the flutter mode meets the minimum damping requirement of 1.5%. The tunable filter is set to $F_{\mathrm{tune}}(s) = 1$.

The controller bandwidth is still limited by the band-pass filter $F_{\mathrm{BPF}}(s)$. The second-order band-pass filter ensures that the controller is primarily active at the frequency of the flutter mode. The specific bandwidth of both benchmark controllers is selected to minimize their actuator usage, refer to subsection 4.3. Through the band-pass filter, the controller has little effect on high-frequency and low-frequency modes, and the stability robustness margins are improved.

The evolution of the poles with this first benchmark controller is visualized in Fig. 10. Improvements in mode damping are visualized as green arrows, and a damping degradation as red arrows. The damping of the flutter mode is increased to 1.5%, but the damping of some of the other modes is reduced. In order to mitigate an adverse damping reduction of residual modes, the method employed for computing the benchmark controllers [4] allows for designing blending controllers in a decoupled way, i.e., the controller can be designed such that it has no influence on the selected residual modes.

This first controller was designed with no decoupling constraint. Indeed, some of the modes were strongly affected, see red/green arrows in Fig. 10. In an attempt to prevent the damping reduction on the mode affected with the lowest damping, an additional decoupling constraint was added for this mode. The results obtained with this second benchmark controller are shown in Fig. 11. The decoupling constraint is indicated with the yellow square. It was satisfied (no impact of the controller on this mode), but at the expense of even more damping reduction on many of the residual modes, see red/green arrows in Fig. 11. Note, that this mode was selected as the resulting coupling with other modes does not lead to a damping decrease of lightly damped modes, but shows the effect of a decoupling constraint on other modes, the actuator

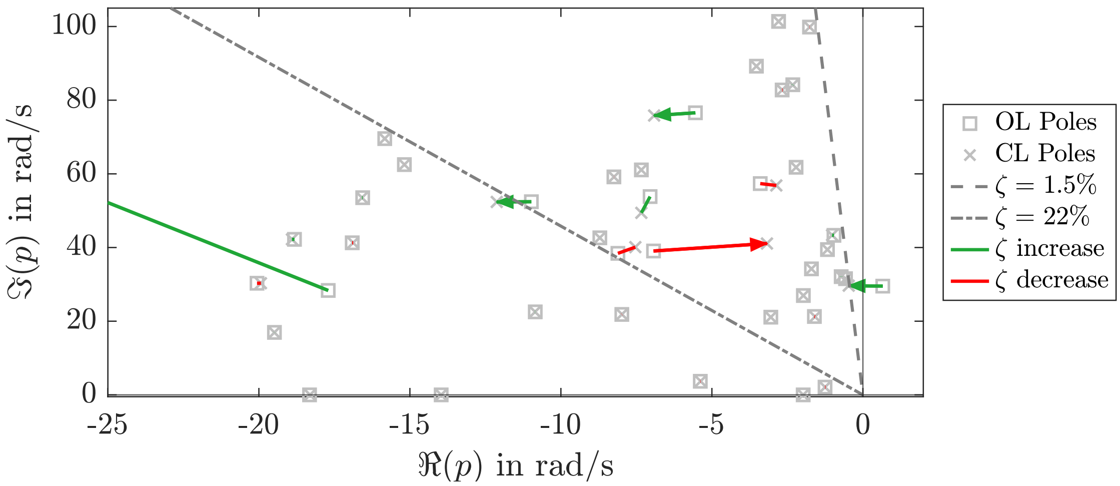

Figure 10: Open-loop (OL) and Closed-loop (CL) poles of first benchmark controller (without decoupling constraints). Controller poles not shown to ease the comparison.

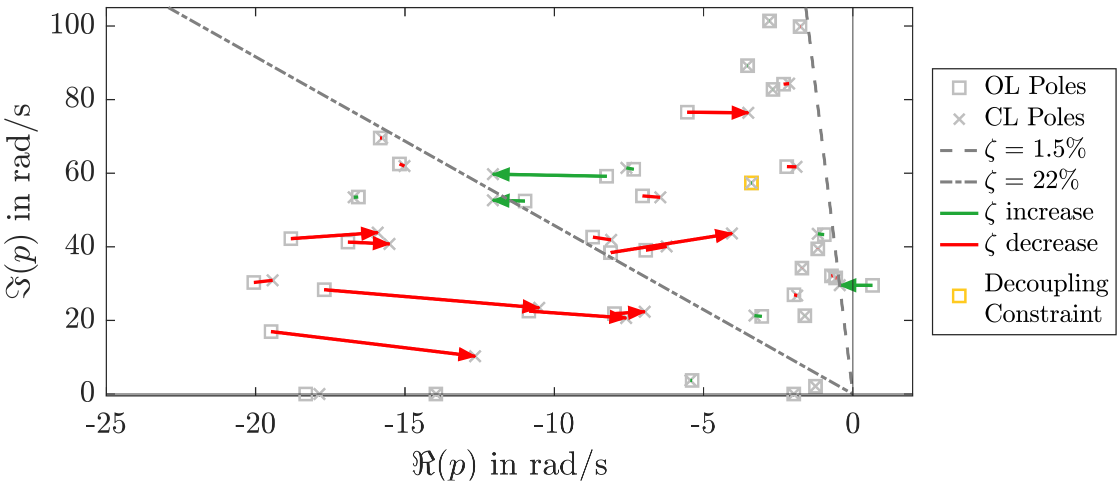

Figure 11: Open-loop (OL) and Closed-loop (CL) poles of second benchmark controller (with one decoupling constraints). Controller poles not shown to ease the comparison. Decoupling constraint imposed on a single mode, highlighted with a yellow square.

activity and stability robustness margins. The decoupling constraint is applied by projecting the input blending vector into the nullspace of the input vector of the selected residual mode.

4.2 Comparison of controller characteristics

For the structured $\mathcal{H}_2/\mathcal{H}_\infty$ controller (tuned with the method proposed in this work), damping lower bound constraints based on the acceleration sensitivity are applied on all low-damped modes, as described in subsection 3.2.3. The flutter (or primary) mode needs to be damped to at least 1.5%, while the other low-damped modes need to remain as damped as in the open-loop case. No constraint was set on the other modes (those having a damping of at least 22% in open-loop).

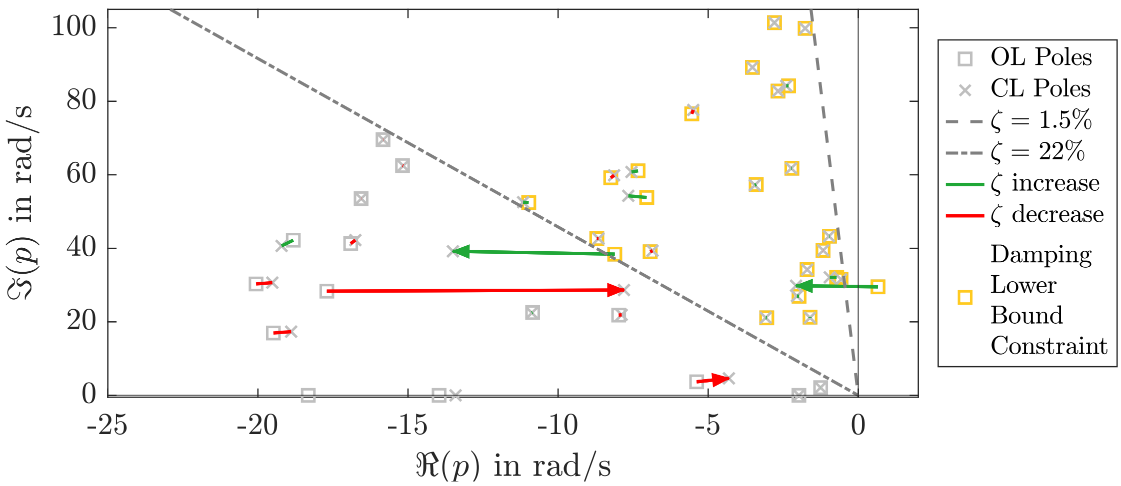

Figure 12: Open-loop (OL) and Closed-loop (CL) poles of structured $\mathcal{H}_2/\mathcal{H}_\infty$ controller. Controller poles not shown to ease the comparison. Damping Lower Bound (DLB) constraints based on Acceleration Sensitivity are imposed on all modes with less than 22% OL damping. DLB is either the damping of the structure itself (1.5%) or the open-loop damping, whichever is greater.

The damping of the low-damped modes (less than 22% OL damping) is largely maintained or increased, see Fig. 12. Minimal decrease can be observed for a few modes, which correspond to cases in which the modes were not perfectly decoupled and so the link between modal specification and $\mathcal{H}_\infty$ norm of the acceleration sensitivity function is not perfect. Overall, the proposed method gives significantly more control of the change in pole location than the input/output blending method on such a system with numerous modes considered at once. Note that the damping of the flutter mode is increased far beyond 1.5%. This behavior is caused by the other tuning requirements, i.e., either to meet the stability robustness requirement or to minimize the actuator activity.

Furthermore, note that the proposed method would allow setting damping lower bounds to values that are smaller than the open-loop damping of the corresponding modes, such that the control design algorithm could potentially trade the damping of residual modes for lower actuator activity. This option was not attempted in this application, as it would have made the comparison with the input/output blending more difficult.

4.2.1 Dynamic and static controller elements

Figure 13 visualizes the values of the blending vectors for all three controllers. All controllers primarily use the anti-symmetric signals as the flutter mode is anti-symmetric in shape. Figure 14 shows the magnitude of the frequency response of $\mathbf{K}_{\text{dyn}}$ for the three controllers. Somewhat surprisingly, the magnitude of the structured $\mathcal{H}_2/\mathcal{H}_\infty$ controller drops off at much lower frequency than the frequency of the flutter mode (29 rad/s), even though the non-tunable filter has a high-pass bandwidth of 10 rad/s.

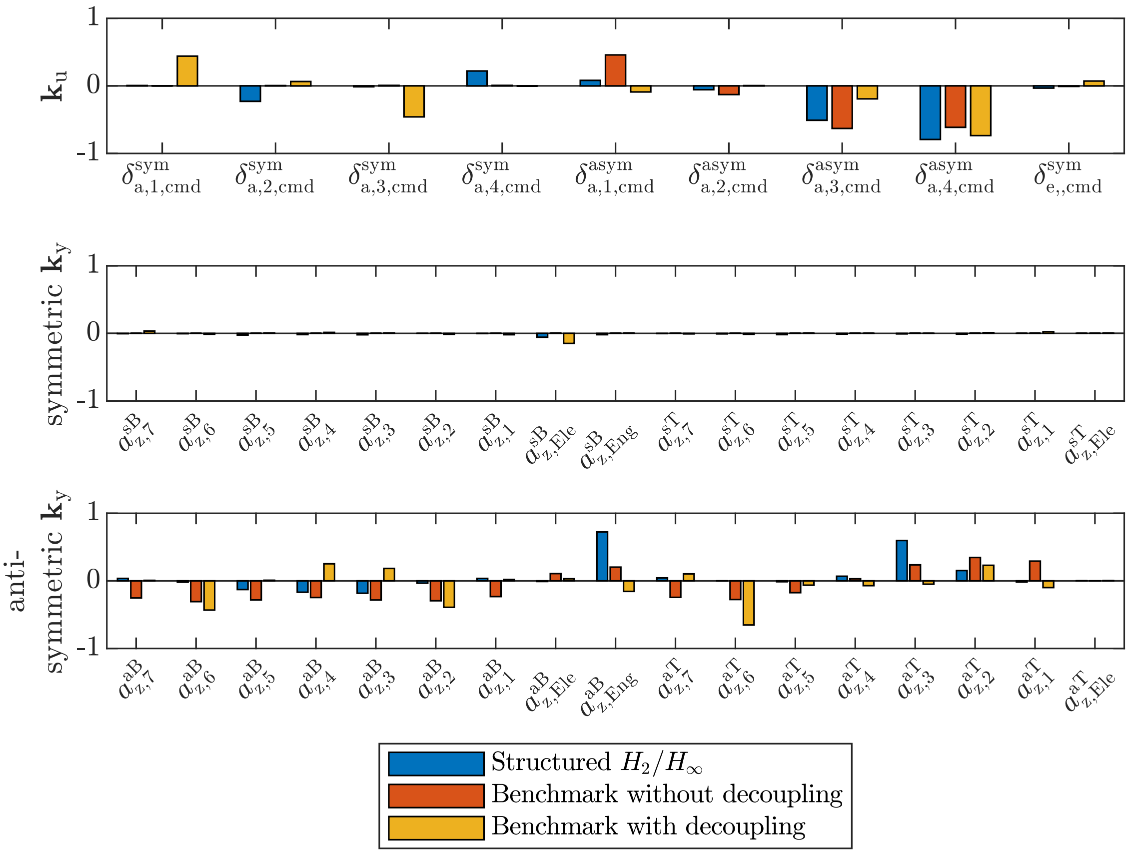

Figure 13: Input and Output Blending vector entries.

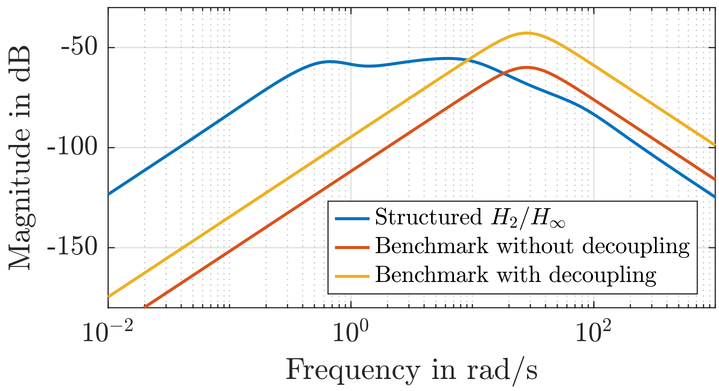

Figure 14: Bode magnitude response of $\mathbf{K}_{\text{dyn}}$ for the structured $\mathcal{H}_2/\mathcal{H}_\infty$ and benchmark controllers.

4.2.2 Actuator usage

Figure 15 shows a comparison of the actuator usage of the controller synthesized with the proposed method and the benchmark controllers in the time-domain, both for a noise excitation through the third anti-symmetric aileron in Fig. 15a or through the fourth anti-symmetric aileron in Fig. 15b. The excitation signal is adopted from the von Kármán turbulence template in [25, AMC25.341b]. These inputs were selected for excitation because all controllers have large entries in $\mathbf{k}_\mathrm{u}$ for at least one of these control surfaces.

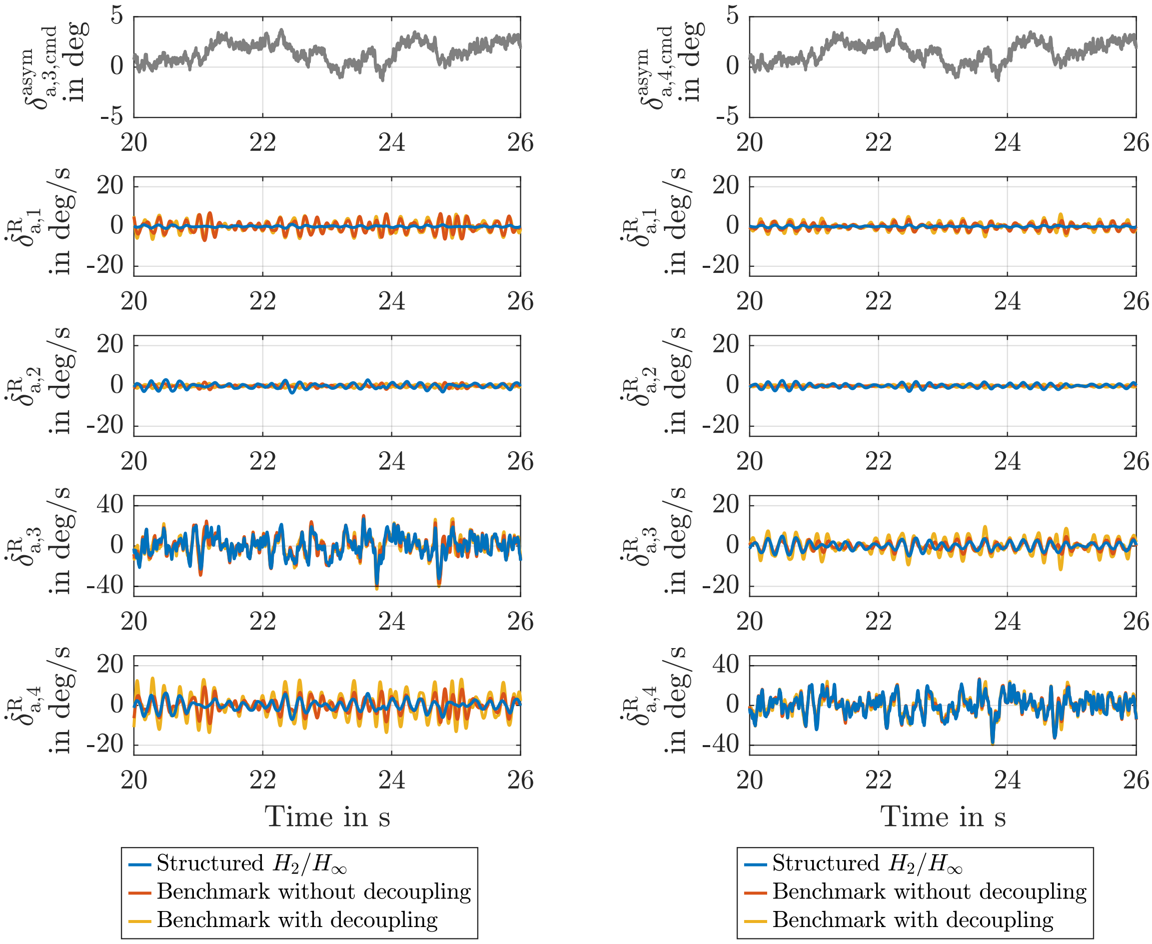

(a) Anti-symmetric deflection of aileron 3 (b) Anti-symmetric deflection of aileron 4

Figure 15: Time domain actuator usage for a dynamic anti-symmetric deflection of aileron 3 or aileron 4. Deflection rate of these actuators elevated as they are used for excitation.

For the most part, the excitation of the third aileron for the case in Fig. 15a, respectively the fourth aileron for Fig. 15b, are the direct consequence of the excitation. The activity of the other control surfaces is significantly lower with the structure $\mathcal{H}_2/\mathcal{H}_\infty$ controller except for the second aileron, with is uses more than benchmark controllers.

Figure 16 shows a comparison of the actuator usage of the controller synthesized with the proposed method and the benchmark controllers in the frequency-domain, both for an excitation through the third anti-symmetric aileron Fig. 16a or through the fourth anti-symmetric aileron Fig. 16b. The observations made in the time domain can also be clearly seen in the frequency responses.

While the three controllers employ a different control strategy, the structured $\mathcal{H}_2/\mathcal{H}_\infty$ controller uses the actuators the least (regarding their deflection rates).

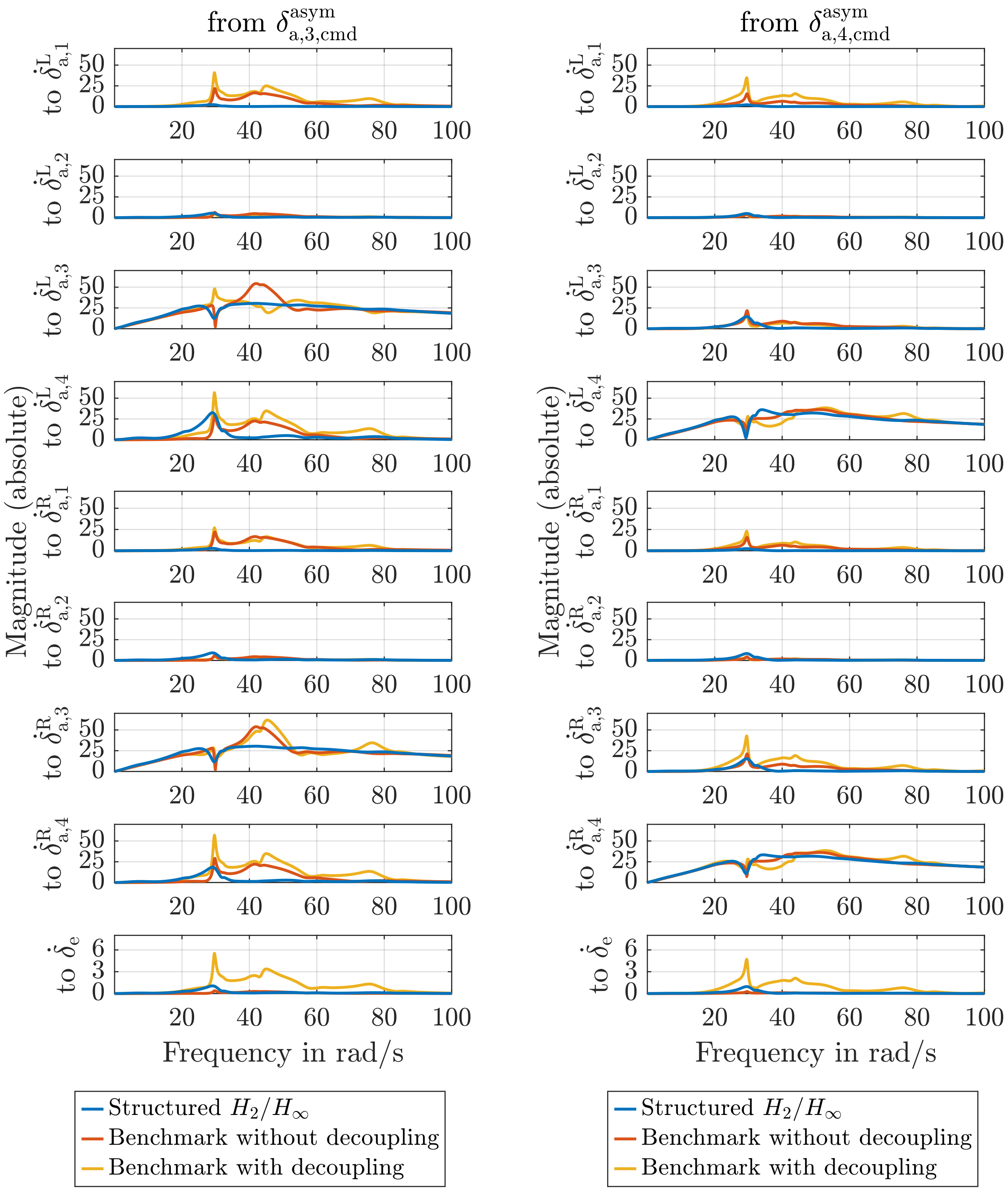

(a) Anti-symmetric deflection of aileron 3 (b) Anti-symmetric deflection of aileron 4

Figure 16: Frequency-domain actuator usage for a dynamic anti-symmetric deflection of aileron 3 or aileron 4.

4.3 Effect of Band-Pass Filter Bandwidth on Benchmark Controller Behavior

The band-pass filter $F_{\text{BPF}}(s)$ is tuned such that the actuator activity is minimized and the stability robustness margins are maximized. Figure 17 visualizes the actuator effort and stability robustness margins for varying band-pass bandwidths of the benchmark controllers. For comparison, the respective values for the structured $\mathcal{H}_2/\mathcal{H}_\infty$ controller are also shown. Its band-pass filter bandwidth is not altered. The actuator activity, measured by the 2-norm of $\mathbf{T}_{\mathbf{d}\to\dot{\boldsymbol{\delta}}_{\text{act}}}$, is normalized to that of the structured $\mathcal{H}_2/\mathcal{H}_\infty$ controller.

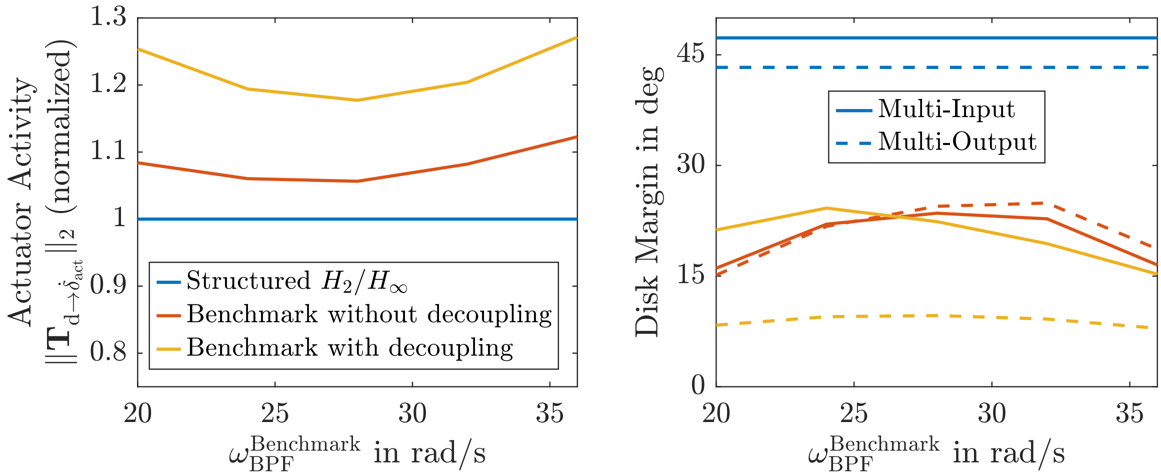

Figure 17: Parameter study of the band-pass-filter bandwidth for the controller regarding actuator usage and stability robustness margins.

The benchmark controllers have minimal actuator activity for a band-pass filter bandwidth centered around 28 rad/s (very close to that of the flutter / primary mode). The selected values of the band-pass filter parameters of the respective controller are summarized in Tab. 2. Note that an increase of the feedback gain yields lower disk margins and increased actuator activity for both benchmark controllers. Overall, the controller designed with the new method outperforms those

Table 2: $F_{\text{BPF}}(s)$ parameters

Controller	ω_{HP}	ω_{LP}
Structured $\mathcal{H}_2/\mathcal{H}_\infty$	10	80
Benchmark without decoupling	28	28
Benchmark with decoupling	28	28

designed with the Input/Output Blending Method presented in [4] regarding the actuator activity. Furthermore, the multi-loop disk margins are doubled with the new method, see Fig. 17, and the damping of all aeroelastic modes is maintained or increased, recall Fig. 12. Applying this large amount of mode damping constraints would not be possible with the decoupling approach of [4] without violating actuator effort and stability robustness requirements.

5 CONCLUSIONS AND GENERAL SIGNIFICANCE

A new approach for designing active flutter controllers using the acceleration sensitivity function to specify damping lower bound constraints was presented. The proposed method focuses on minimizing the actuator activity (only optimization objective) under these damping constraints as well as robustness stability constraints. The method can certainly be extended in many ways and can be applied to even larger problems (e.g., with more system uncertainties and considering gain scheduling). In this work, the focus has rather been put on comparing this approach with prior work in active flutter control/suppression. In particular, the input/output blending approach from [4, 18] and the robust modal control approach from [13] are two interesting approaches for this comparison.

The comparison with [4, 18] is interesting, as this approach also focused heavily on preventing adverse coupling with the residual modes (i.e., the ones that the flutter controller is not supposed to affect in damping). The constraints based on the acceleration sensitivity function can be used to avoid destabilizing the residual modes. As already discussed in great detail by the authors in [5], enforcing a perfect decoupling with the residual modes goes rather beyond the actual requirements for the design of a flutter controller and it makes sense to relax the decoupling constraints. The input/output blending is mathematically elegant and understanding this concept is recommended for any designer of flutter controllers because it shows very well the connection between mode shapes and the modal observability and controllability. However, scaling up this concept to complex aircraft configurations seems hardly possible as the constraints can only be applied to a limited number of modes, depending on the number of actuators and sensors available for flutter control. Controlling to which extent other modes are impacted is difficult even with the approach from [5]. Guidelines for including dynamic filters are provided in [18] as mean for designing dynamic controllers, but it seems that it will hardly be as powerful as the frequency-domain design techniques as proposed in [13] and the present work.

The comparison with [13] is interesting because both methods share the core idea of using the link between specific transfer function norms and the damping of the second-order modes. Actually, the selected transfer functions are very similar and differ largely in the chosen output: the exogenous output being the modal velocity in [13], and in the present work the modal acceleration. For the proposed method, the control synthesis is performed with a structured $\mathcal{H}_2/\mathcal{H}_\infty$ scheme. This allows the design of a reduced order controller and to use a multi-channel design with an $\mathcal{H}_2$ objective function, disk margins, and numerous $\mathcal{H}_\infty$ constraints for the modal damping constraints. A more classical full-order $\mathcal{H}_\infty$ control design scheme was used in [13]. The choice of the transfer function for the damping constraints/objectives and the robust control technique are two relatively unrelated differences, such that a number of variations of both methods could be made.

With all the imperfections that such a comparison may present, Table 3 attempts to give a summary of the main differences in properties between the active flutter control approaches from [4], from [13], and from this work.

The systune framework, used for synthesizing the structured $\mathcal{H}_2/\mathcal{H}_\infty$ controller, employs a non-smooth optimization technique [15]. This can handle systems with more than 100 states efficiently and effectively. The low-order controller may, however, correspond to a local optimum. Hence, it is common practice to restart the control synthesis with random initial values to try to achieve a solution closer to the global optimum. This can lead to a large controller synthesis computational time. The synthesis of the structured $\mathcal{H}_2/\mathcal{H}_\infty$ controller had a runtime of multiple hours on consumer-grade laptop, while the synthesis of the benchmark controllers with the method from [4] takes only milliseconds.

Table 3: Comparison of the considered active flutter control methods ('good': green, 'neutral': orange, 'bad': red).

Category	**Input/Output Blending for Modal Velocity Feedback (MVF) [4]**	**Acceleration-to-velocity-based modal full-order $\mathcal{H}_\infty$ synthesis [13]**	**Proposed method: Actuator-friendly acceleration-sensitivity-based modal structured $\mathcal{H}_2/\mathcal{H}_\infty$ synthesis**
Controller synthesis computational effort	Very low (mostly linear algebra)	Medium (full-order H_∞ synthesis, typically $\mathcal{O}(n_x^4)$)	High (synthesis takes long and may require several starts with different initial conditions)
Controller type	Proportional blending feedback (can be changed, but could become rapidly complicated)	Full-order output feedback	Dynamic blending feedback (structure can be changed easily)
Tunable controller parameters	$n_\mathrm{u} + n_\mathrm{y} + 1$	$(n_\mathrm{u} + n_\mathrm{x})(n_\mathrm{y} + n_\mathrm{x})$	$n_\mathrm{u}+n_\mathrm{y}+(n_{\mathrm{x,tune}}+1)^2$
Control activity	High, when decoupling constraints are applied	Can be low (combined designed with other objectives, depends on tuning)	As low as possible for given damping / robustness constraints (only objective)
Stability Robustness Margins measured by multi-loop Disk Margins (DM)	Not controlled a priori. Expected fairly low when decoupling constraints are applied.	High (Robustness considered through input disturbance, DM not directly specified)	As high as physically possible given other constraints: DM can be directly specified (feature of systune)
Type of decoupling constraint for residual aeroelastic modes	No change of pole location (neither in damping or frequency)	Damping indirectly constrained via upper bound on real part of the modes pole (velocity sensitivity)	Damping directly constrained by a lower bound, (acceleration sensitivity)
Number of residual aeroelastic modes that can be considered	$\frac{n_\mathrm{u} - 2}{2}$ or $\frac{n_\mathrm{y} - 2}{2}$	Arbitrary, as long as the problem is feasible.	Arbitrary, as long as the problem is feasible.

The structured $\mathcal{H}_2/\mathcal{H}_\infty$ controller is tuned for a single plant only in this work. It could also be tuned and evaluated with multiple plants at once. This is especially interesting for considering variations in parameters that are not part of the gain scheduling. For example, usually the mass distribution cannot be measured reliably and would not be used for gain scheduling: the controller has to provide the desired level of damping regardless of the mass distribution.

A similar scheme to the one presented in [30] could be used to schedule the gains over the flight points (these parameters can be measured reliably) to further reduce the actuator usage. Considering multiple plants in the controller design instead of a single one is straightforward with systune. If the set of models sufficiently covers system variations / uncertainties (mass distribution, mode shape, operating point) one could also relax the damping requirement from $\zeta_{\mathrm{LB,i}} = \max(\zeta_{\mathrm{FE,i}}, \zeta_{\mathrm{OL,i}})$ to $\zeta_{\mathrm{LB,i}} = \zeta_{\mathrm{FE,i}}$ (or some intermediate value) to potentially reduce the actuator usage further.

ACKNOWLEDGMENTS

We would like to acknowledge the funding by the Deutsche Forschungsgemeinschaft (DFG, German Research Foundation) under Germany's Excellence Strategy – EXC 2163/1 - Sustainable and Energy Efficient Aviation – Project-ID 390881007.

6 REFERENCES

[1] Livne, E. (2018). Aircraft active flutter suppression: State of the art and technology maturation needs. *Journal of Aircraft*, 55(1), 410–452, doi: 10.2514/1.C034442.

[2] Wykes, J. H., Borland, C. J., Klepl, M. J., et al. (1977). Design and development of a structural mode control system. Tech. rep., NASA, `https://ntrs.nasa.gov/citations/19770026257`. NASA CR-143846.

[3] Wykes, J. H., Byar, T. R., MacMiller, C. J., et al. (1980). Aanlyses and tests of the b-1 aircraft structural model control system. Tech. rep., NASA, `https://ntrs.nasa.gov/citations/19800006814`. NASA CR-144887.

[4] Pusch, M. and Ossmann, D. (2019). Blending of inputs and outputs for modal velocity feedback. In *27th Mediterranean Conference on Control and Automation (MED)*. pp. 530–535, doi: 10.1109/MED.2019.8798491.

[5] Strohteicher, T. and Fezans, N. (2026). Relaxation of input/output-blending decoupling constraints with application to flutter control. In *Proceedings of the 2026 CEAS EuroGNC conference*. Madrid, Spain, doi: 10.82124/CEAS-GNC-2026-071.

[6] Adams, J., W. M. and Tiffany, S. H. (1984). Design of a candidate flutter suppression control law for DAST ARW-2. Tech. rep., NASA, `https://ntrs.nasa.gov/citations/19840021814`. NASA-TM-86257.

[7] Fezans, N., Alazard, D., Imbert, N., et al. (2010). Robust LPV control design for a RLV during reentry. In *AIAA Guidance, Navigation, and Control Conference*. doi: 10.2514/6.2010-8194.

[8] Fezans, N., Alazard, D., Imbert, N., et al. (2008). H_∞ control design for generalized second order systems based on acceleration sensitivity function. In *16th Mediterranean Conference on Control and Automation*. pp. 1508–1513, doi: 10.1109/MED.2008.4602153.

[9] Fezans, N., Alazard, D., Imbert, N., et al. (2007). H_∞ control design for multivariable mechanical systems - application to RLV reentry. In *AIAA Guidance, Navigation, and Control Conference*. doi: 10.2514/6.2007-6349.

[10] Guy, N., Alazard, D., Cumer, C., et al. (2013). A new attitude control design approach for flexible satellites. *IFAC Proceedings Volumes*, 46(19), 500–505. ISSN 1474-6670, doi: 10.3182/20130902-5-DE-2040.00098. 19th IFAC Symposium on Automatic Control in Aerospace.

[11] Alazard, D. (2013). Reverse engineering for mechanical systems. In *Reverse Engineering in Control Design*, chap. 3. John Wiley Sons, Ltd. ISBN 9781118603932, pp. 77–134, doi: 10.1002/9781118603932.ch3.

[12] Perez, J. A., Pittet, C., Alazard, D., et al. (2016). Integrated control/structure design of a large space structure using structured H_∞ control. *IFAC-PapersOnLine*, 49(17), 302–307. ISSN 2405-8963, doi: 10.1016/j.ifacol.2016.09.052. 20th IFAC Symposium on Automatic Control in Aerospace ACA 2016.

[13] Theis, J., Pfifer, H., and Seiler, P. (2020). Robust modal damping control for active flutter suppression. *Journal of Guidance, Control, and Dynamics*, 43(6), 1056–1068, doi: 10.2514/1.G004846.

[14] Gahinet, P. and Apkaria, P. (2011). Structured H_∞ synthesis in MATLAB. In *18th International Forum of Automated Control (IFAC) World Congress*, vol. 44. p. 1435–1440, doi: 10.3182/20110828-6-IT-1002.00708.

[15] Apkarian, P. and Noll, D. (2017). The H_∞ control problem is solved. *Aerospace Lab*, 13(1), doi: 10.12762/2017.AL13-01.

[16] Waitman, S. and Marcos, A. (2019). Active flutter suppression: non-structured and structured H_∞ design. *IFAC-PapersOnLine*, 52(12), 146–151. ISSN 2405-8963, doi: https://doi.org/10.1016/j.ifacol.2019.11.184. 21st IFAC Symposium on Automatic Control in Aerospace (ACA 2019).

[17] Faïsse, E., Vernay, R., Vetrano, F., et al. (2021). Adding control in multidisciplinary design optimization of a wing for active flutter suppression. In *AIAA SciTech Forum*. AIAA, doi: 10.2514/6.2021-0892.

[18] Pusch, M. (2020). *Blending of Inputs and Outputs for Modal Control of Aeroelastic Systems*. PhD Thesis, Technical University Hamburg, `https://elib.dlr.de/139100/`.

[19] Wöhler, S., Häßy, J., and Kriewall, V. (2024). Establishing the DLR-F25 as a research baseline aircraft for the short-medium range market in 2035. In *34th Congress of the International Council of the Aeronautical Sciences, ICAS*. Florence, Italy, `https://www.icas.org/icas_archive/icas2024/data/preview/icas2024_0398.htm`.

[20] Streitenberger, K. M. and Feldwisch, J. M. (2025). CFD-based aeroelastic maneuver and gust loads analysis for a high aspect ratio wing configuration. In *AIAA SCITECH 2025 Forum*. Orlando, doi: 10.2514/6.2025-1663.

[21] Fehrs, M., Micheli, B., Kaiser, C., et al. (2026). Aeroelastic damping augmentation and flutter analysis for a high-aspect-ratio wing aircraft in the transonic flight regime. In *International Forum on Aeroelasticity and Structural Dynamics 2026 (IFASD)*. Göttingen, Deutschland.

[22] Thormann, R. and Widhalm, M. (2013). Linear-frequency-domain predictions of dynamic-response data for viscous transonic flows. *AIAA Journal*, 51(11), 2540–2557, doi: 10.2514/1.J051896.

[23] Mayo, A. J. and Antoulas, A. C. (2007). A framework for the solution of the generalized realization problem. *Linear Algebra and its Applications*, 425, 634–662, doi: 10.1016/j.laa.2007.03.008.

[24] Quero, D., Vuillemin, P., and Poussot-Vassal, C. (2019). A generalized state-space aeroservoelastic model based on tangential interpolation. *Aerospace*, 6(1), 9, doi: 10.3390/aerospace6010009.

[25] EASA (2023). CS-25: Certification specifications and acceptable means of compliance for large aeroplanes. Amendment 27, European Union Aviation Safety Agency.

[26] Kailath, T. (1980). *Linear Systems*, vol. 156. Prentice-Hall Englewood Cliffs, NJ, USA. ISBN 978-0135369616.

[27] MathWorks (2023). Control system toolbox R2023b. Tech. rep., The MathWorks, Inc.

[28] Skogestad, S. and Postlethwaite, I. (2005). *Multivariable Feedback Control: Analysis and Design*. New York: Wiley & Sons, 2^{nd} ed. ISBN 978-0-470-01167-6.

[29] Seiler, P., Packard, A., and Gahinet, P. (2020). An introduction to disk margins. *IEEE Control Systems Magazine*, 40(5), doi: 10.1109/MCS.2020.3005277.

[30] Strohteicher, T. and Fezans, N. (2026). Combined design of gain-scheduled C-star and maneuver load alleviation laws. *Journal of Guidance, Control, and Dynamics (online pre-publication)*, 1–12, doi: 10.2514/1.G009267.

COPYRIGHT STATEMENT